coatings

MDPI

Article

Exploring TMA and H_2O Flow Rate Effects on Al_2O_3 Thin Film Deposition by Thermal ALD: Insights from Zero-Dimensional Modeling

Júlia Karnopp [1,*], Nilton Azevedo Neto [1], Thaís Vieira [1], Mariana Fraga [2], Argemiro da Silva Sobrinho [1], Julio Sagás [3] and Rodrigo Pessoa [1,*]

[1] Plasmas and Processes Laboratory, Aeronautics Institute of Technology (ITA), São José dos Campos 12228-900, SP, Brazil; nilton.azevedo@unesp.br (N.A.N.); vieira.thaism@gmail.com (T.V.); argemiro@ita.br (A.d.S.S.)
[2] School of Engineering, Mackenzie Presbyterian University, São Paulo 01221-040, SP, Brazil; mafraga@ieee.org
[3] Laboratory of Plasmas, Films and Surfacnies, Santa Catarina State University (UDESC), Joinville 89219-710, SC, Brazil; julio.sagas@udesc.br
* Correspondence: julia_karnopp@outlook.com (J.K.); rspessoa@ita.br (R.P.); Tel.: +55-12-3947-5875 (R.P.)

Abstract: This study investigates the impact of vapour-phase precursor flow rates—specifically those of trimethylaluminum (TMA) and deionized water (H_2O)—on the deposition of aluminum oxide (Al_2O_3) thin films through atomic layer deposition (ALD). It explores how these flow rates influence film growth kinetics and surface reactions, which are critical components of the ALD process. The research combines experimental techniques with a zero-dimensional theoretical model, designed specifically to simulate the deposition dynamics. This model integrates factors such as surface reactions and gas partial pressures within the ALD chamber. Experimentally, Al_2O_3 films were deposited at varied TMA and H_2O flow rates, with system conductance guiding these rates across different temperature settings. Film properties were rigorously assessed using optical reflectance methods and attenuated total reflectance-Fourier transform infrared (ATR-FTIR) spectroscopy. The experimental findings revealed a pronounced correlation between precursor flow rates and film growth. Specifically, at 150 °C, film thickness reached saturation at a TMA flow rate of 60 sccm, while at 200 °C, thickness peaked and then declined with increasing TMA flow above this rate. Notably, higher temperatures generally resulted in thinner films due to increased desorption rates, whereas higher water flow rates consistently produced thicker films, emphasizing the critical role of water vapour in facilitating surface reactions. This integrative approach not only deepens the understanding of deposition mechanics, particularly highlighting how variations in precursor flow rates distinctly affect the process, but also significantly advances operational parameters for ALD. These insights are invaluable for enhancing the application of ALD technologies across diverse sectors, including microelectronics, photovoltaics, and biomedical coatings, effectively bridging the gap between theoretical predictions and empirical results.

Keywords: atomic layer deposition; aluminum oxide; kinetics modelling; precursor flow rate

Citation: Karnopp, J.; Neto, N.A.; Vieira, T.; Fraga, M.; Sobrinho, A.d.S.; Sagás, J.; Pessoa, R. Exploring TMA and H_2O Flow Rate Effects on Al_2O_3 Thin Film Deposition by Thermal ALD: Insights from Zero-Dimensional Modeling. *Coatings* **2024**, *14*, 578. https://doi.org/10.3390/coatings14050578

Academic Editor: Simona Căprărescu

Received: 10 April 2024
Revised: 29 April 2024
Accepted: 3 May 2024
Published: 7 May 2024

1. Introduction

Thin films play a crucial role in enhancing the surface properties of various materials. One of the key techniques in this domain is atomic layer deposition (ALD), a vapour-phase deposition method characterized by its layer-by-layer mechanism and self-limiting chemisorption of reactants [1]. ALD is distinguished by its precise control over atomic-scale layer growth, enabling the production of uniform and conformal coatings. These qualities make it indispensable in micro/nanoelectronics and other fields [2,3]. ALD operates through a cyclical process, sequentially exposing the substrate to vapour-phase precursors. These precursors react with the substrate's surface, alternating with purge periods that

remove byproducts and excess gases. A common example is the deposition of alumina (Al_2O_3), where a typical cycle involves exposure to a metal precursor, purging, oxidation, and another purging step.

The ALD Al_2O_3 process, particularly using trimethylaluminum (TMA) and water, is a well-studied ALD application. This combination is known for its robust chemical kinetics and ideal surface saturation properties, making it a benchmark in ALD research [4,5]. The Al_2O_3 films obtained through ALD exhibit dielectric and amorphous properties [6–8]. They are widely applied in various fields, including electronic device manufacturing, photovoltaic cell production, corrosion protection coatings, and biomedical applications [7,9–11].

Extensive experimental and theoretical research has been conducted on the thermal ALD process of Al_2O_3, focusing on the effects of various process parameters such as precursor exposure time (or dose), purge time, and process temperature [12,13]. Theoretical work, which has become increasingly central to ALD research, plays a crucial role in understanding and refining experimental procedures. It provides insights often challenging to obtain through experimental methods alone. Theoretical models, developed at various scales, include atomic-scale models that simulate the film growth process and study fluid dynamics within the system. At the atomic scale, models based on density functional theory (DFT) have been used to simulate and elucidate the chemical mechanisms occurring on the surface [14–18]. These models are instrumental in investigating the impact of ALD process parameters on aspects like film growth, thickness, and growth per cycle (GPC). A few models that leverage fluid dynamics are used to simulate the ALD process in a three-dimensional context [19–21]. These fluid dynamics models, or those involving transport phenomena, can become computationally and mathematically complex depending on the system geometry, requiring increased computational capacity [17,20,22,23].

Models that simulate film growth are particularly critical for elucidating the chemical mechanisms at play during deposition and how they are influenced by various process parameters [14,24,25]. Models focusing on surface kinetics often require integration with fluid dynamics information within the reactor and are typically coupled with a fluid dynamics model [14,21]. This coupling can increase the model's complexity and computational demands. One strategy to simplify the model is to eliminate the spatial dependence of variables using a zero-dimensional approach. However, no zero-dimensional model currently in the literature simulates the entire ALD Al_2O_3 deposition process, including the calculation of the partial pressure of precursors and CH_4, a byproduct of the surface reactions. While such models do not provide information about the spatial variation in parameters, they can be solved more easily computationally and enable the simulation of how parameters affect film growth. For these models, it is necessary to assume uniform distribution of the precursor throughout the chamber volume and that film growth strictly adheres to the surface, which is a reasonable assumption for the ALD process.

Despite the advancements in theorical studies for Al_2O_3 ALD films, substantial opportunities still exist for further exploration in the modelling of ALD, particularly in the case of investigating the effects of precursor flow rate on the process mechanisms that remain underexplored. This parameter, critical in vapour-phase deposition, is often overlooked and unreported in standard ALD procedures, likely due to the difficulty in directly measuring vapours from complex liquid or solid precursors. Matero et al. investigated how water dose affects the growth rate of ALD-deposited Al_2O_3 using TMA and H_2O. Increasing the water dose enhanced growth, likely due to more hydroxyl groups on the film surface, without impacting the film's composition or electrical and optical properties [12]. Notably, Kuse et al.'s study on ALD of Al_2O_3 on Si(001) using TMA and H_2O [26] highlighted that the film growth rate was impacted by TMA and H_2O partial pressures. Their results indicate that higher precursor concentrations lead to increased surface site conversion and film growth per ALD cycle, but also result in greater aluminium silicate formation at the Al_2O_3/Si(001) interface.

In developing a zero-dimensional model for ALD deposition, it is essential to specify the gas flow rates of the precursors and nitrogen (N_2) gas, which is used for purging and

carrying the precursors. Given the challenges in measuring substance flow in the vapour phase, particularly with time resolution compatible with an ALD pulse, we propose an indirect method of measurement. This method involves estimating the flow rates through monitoring the partial pressures of the precursors and the system's capacitance.

This study thoroughly investigates the impact of varying TMA flow rates on the Al_2O_3 deposition process using TMA and water precursors. To model Al_2O_3 deposition by ALD with less complexity, we modified a kinetic model originally developed by Gakis et al. [15] and used it as the basis for our investigation. This model was adapted to specifically analyze the chemical mechanisms occurring during the deposition process when varying the TMA and H_2O flow rates. A zero-dimensional balance equation system was included to calculate the partial pressure of the precursor and of the nitrogen used for purging, as well as the CH_4 byproduct of surface reactions. Our simulation results were compared with experimental outcomes to validate the model's accuracy and relevance in practical scenarios.

2. Surface Chemistry

The deposition of Al_2O_3 thin films by ALD, utilizing TMA and H_2O as precursors, involves a series of surface reactions. These reactions are well described by the overall chemical equation [3,18,27]:

$$2Al(CH_3)_3 + 3H_2O \rightarrow Al_2O_3 + 6CH_4. \quad (1)$$

This process entails the formation of stable Al_2O_3 molecules on the surface and CH_4 molecules in the gas phase. Each precursor cycle can be analysed separately. Initially, TMA molecules in the gas phase adsorb onto the surface hydroxyl (OH) groups [3,28]. The TMA adsorption is reversible and an exothermal process [18]. Once adsorbed, TMA can either desorb or react with OH, forming dimethylaluminium (DMA) on the surface (Figure 1) [18]:

$$||-OH + Al(CH_3)_2 \rightarrow ||-O-Al(CH_3)_2 + CH_4 \quad (2)$$

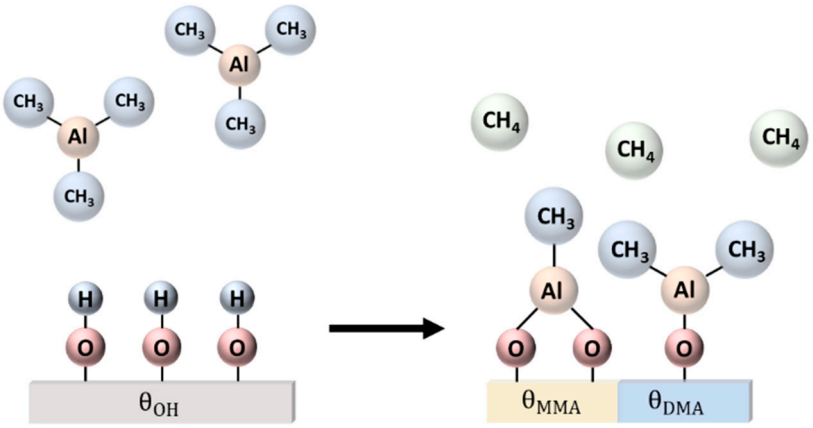

Figure 1. Schematics of the chemical mechanism during the TMA pulse.

The reaction step involving TMA is endothermic and exhibits an activation barrier. In this process, a methyl group from TMA reacts with a hydroxyl group to form a methane molecule, CH_4, which then desorbs into the gas phase [3,18]. Regarding the second reaction, which involves DMA on the surface, the proposed pathways have been evaluated. The most likely pathway, characterized by the lowest reaction barrier energy, involves a direct reaction with an adjacent OH site [18]. Consequently, DMA can react with a neighbouring OH site, leading to the production of another CH_4 molecule and the formation of monomethylaluminum (MMA) on the surface, as illustrated in Figure 1.

$$||-O-Al(CH_3)_2 + ||-OH \rightarrow (||-O)_2 - Al(CH_3) + CH_4. \quad (3)$$

These reactions continue until the surface reaches saturation. Subsequently, any unreacted TMA and the generated CH_4, both present in the gas phase, are purged from the reactor. Following the TMA pulse, the surface becomes coated with DMA and MMA, both featuring CH_3 terminations. This is clearly illustrated in Figure 1.

During the water pulse, H_2O molecules in the gas phase adsorb exothermically onto the CH_3 terminations of DMA [27]. The absorption is reversible, where the H_2O molecule can either desorb or react with the methyl group. The reaction produces the species called MMAOH on the surface (Figure 2). CH_4 is produced and desorbed in the gas phase, and desorbs from the surface [18,28].

$$||-O-Al(CH_3)_2 + H_2O \rightarrow ||-O-Al(CH_3)OH + CH_4. \quad (4)$$

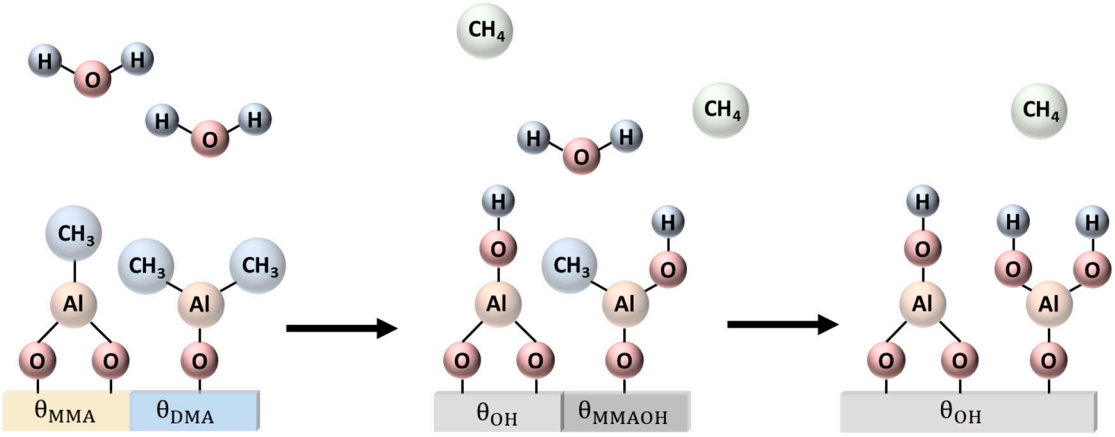

Figure 2. Schematics of the chemical mechanism during the H_2O pulse.

A second H_2O molecule can adsorb onto MMAOH, leading to subsequent reactions. This water may either desorb or undergo a reaction with a CH_3 group in MMAOH. This reaction results in the release of CH_4 as a product, which then desorbs, leaving the surface with an OH-termination:

$$||-O-Al(CH_3)OH + H_2O \rightarrow ||-O-Al(OH)_2 + CH_4. \quad (5)$$

Additionally, water can adsorb onto monomethylaluminum and subsequently react with the methyl group. The adsorption of water is a reversible process, allowing the water to either desorb or react with the methyl group. This reaction, which has a lower activation energy compared to that for DMA, produces OH sites on the surface. This is followed by the formation and desorption of CH_4, as depicted in Figure 2.

$$(||-O)_2-Al(CH_3) + H_2O \rightarrow (||-O)_2-Al-OH_{(s)} + CH_4. \quad (6)$$

Upon completion of the water pulse, the surface is covered with OH groups (Figure 2), ready to react with TMA in the subsequent precursor pulse. Gas-phase species within the reactor, such as unreacted precursor molecules and CH_4, are removed during the next purge.

3. Atomic Layer Deposition Model

3.1. Surface Kinetic Model

The model encompasses a surface kinetic framework that employs a system of differential equations. These equations describe the surface coverage fractions of the species present on the surface, drawing upon the approach proposed by Gakis et al. (2019). In this study, modifications were made to the Gakis et al. model [14]. Specifically, the differential equations were altered to calculate surface coverage fractions instead of species concentrations. Our surface kinetic model was coupled with an additional set of differential

equations, accounting for the partial pressures of gases in the chamber, including TMA, H_2O, CH_4, and N_2. The aim was to develop a simplified model that required lower computational resources to simulate the ALD process. Gakis et al. integrated their model with a computational fluid dynamics (CFD) model to investigate the impact of reactor design and transport phenomena on ALD; our approach differed [14].

We assumed that reactions between the precursor and the surface species occur both during the precursor pulse and the subsequent purge, in contrast to Gakis et al.'s model, where reactions occurred only during the pulse. Additionally, we updated some input parameters, such as the activation energy of reactions and desorption, to align with the findings of Weckman and Laasonen (2015) [18], whose results more closely matched experimental observations regarding the effects of temperature and gas flow rate on film thickness.

We adopted the same surface reactions as Gakis et al. (2019). During the TMA pulse (Equation (7)), we assumed that MMA and DMA were to be generated in equivalent ratios, maintaining the stoichiometry where two molecules of TMA interacted with three molecules of water, resulting in one molecule of Al_2O_3. During the oxidation pulse, water was able to react with DMA, MMA, or MMAOH (Equations (8)–(10)). To solve the models, we considered the intermediate species ($MMAH_2O$, $DMAH_2O$, $MMA(OH)H_2O$) produced on the surface due to precursor adsorption, and the differential equations were solved accordingly.

$$2TMA_{(g)} + 3OH_{(s)} \rightarrow 2TMA_{(ads)} \rightarrow DMA_{(s)} + MMA_{(s)} + 3CH_{4(g)} \quad (7)$$

$$H_2O_{(g)} + MMA_{(s)} \leftrightarrow MMAH_2O_{(s)} \rightarrow Al - OH_{(s)} + CH_{4(g)} \quad (8)$$

$$H_2O_{(g)} + DMA_{(s)} \leftrightarrow DMAH_2O_{(s)} \rightarrow MMAOH_{(s)} + CH_{4(g)} \quad (9)$$

$$H_2O_{(g)} + MMAOH \leftrightarrow MMA(OH)H_2O_{(s)} \rightarrow Al - (OH)_{2(s)} + CH_{4(g)} \quad (10)$$

The surface species covering the substrate included $MMAH_2O$, $DMAH_2O$, $MMA(OH)H_2O$, $TMA_{(ads)}$, DMA, MMA, MMAOH, and OH. The surface coverage fraction of each species k was denoted as θ_k. In our model, we assumed that the surface initially begins fully covered by OH sites, denoted as $\theta_{OH,i} = 1$. Contrary to the approach in Gakis et al. (2019), where the coverage fraction of OH was determined by a balance equation for surface concentration, our model calculated θ_{OH} based on the dynamics changes in surface coverage resulting from ongoing reactions.

$$\Theta_{OH} = 1 - \theta_{DMA} - \theta_{MMA} - \theta_{MMAOH} - \theta_{MMAH_2O} - \theta_{DMAH_2O} - \theta_{MMA(OH)H_2O} \quad (11)$$

This implies that the number of available sites on the surface was equivalent to the number of OH sites at the commencement of deposition. The maximum concentration of OH on the surface can be expressed as a function of substrate temperature, in $mol.m^{-2}$. This relationship was implemented in the studies by Gakis et al. (2019), and it was based on data reported by Haukka and Root (1994) [14,29].

$$C_T = C_{OH} = -2.1661.10^{-8}T + 1.6893.10^{-5}. \quad (12)$$

The concentration of each species on the surface was related to its coverage fraction, which can be expressed by the following equation:

$$\theta_k = \sigma_k \frac{C_k}{C_T}, \quad (13)$$

where σ_k represents the number of sites occupied by species k on the surface.

The coverage fraction of the other species was calculated using a differential balance equation that accounted for the rates of adsorption, desorption, and reaction, as given by the following:

$$\frac{C_T}{\sigma_k}\frac{d\theta_k}{dt} = R_{ads,i} - R_{des,i} - R_{r,i} \quad (14)$$

The precursors in the gas phase absorbed onto the surface at a rate denoted as $R_{ads,I}$, expressed in mol.m^{-2}s^{-1}:

$$R_{ads,i} = s_i F_i, \tag{15}$$

where the species i can either be H_2O or TMA. The term s_i represents the sticking coefficient, and F_i denotes the molar flux. The sticking coefficient is defined as the probability that an incoming molecule will remain attached to the surface [14].

$$s_i = s_{0,i}(1 - \theta_k)e^{-\frac{E_{ads}}{k_b T}}, \tag{16}$$

where E_{ads} is the adsorption activation energy, k_b is the Boltzmann constant, and $s_{0,k}$ denotes the pre-exponential factor of the sticking coefficient.

It was assumed that the gases would behave ideally, and their flux to surface, in mol.s^{-1}m^{-2}, can be described by the Hertz-Knudsen equation:

$$F_i = \frac{P_i}{\sqrt{2\pi M_i RT}}, \tag{17}$$

where P_i and M_i represent the partial pressure, in Pa, and the molar mass of species i, in kg.mol^{-1}, respectively. R denotes the ideal gas constant, and T is the substrate temperature in K. The partial pressure was determined using differential equations for the gas species, which will be described in Section 3.2.

The adsorbed molecules can either desorb or react on the surface. The desorption rate of species i is given in mol.m^{-2}s^{-1} by the following expression:

$$R_{des,i} = k_{des,i} C_i, \tag{18}$$

where $k_{des,i}$ is the desorption rate constant for species i, expressed in s^{-1}. The reaction rate is expressed as follows:

$$R_{r,i} = k_{r,i} C_i, \tag{19}$$

where $k_{r,i}$ is the reaction rate constant.

The rate constants for both adsorption and desorption were calculated using the Arrhenius equation:

$$k_{x,i} = Ae^{-\frac{E_{x,i}}{k_b T}}. \tag{20}$$

Here, $E_{x,i}$ represents the activation energy for the reaction or desorption of species i. The pre-exponential frequency factor, A, for both reaction and desorption, was defined as follows:

$$A = \frac{k_b T}{h_p}, \tag{21}$$

where h_p is the Planck constant [14].

The film thickness, h, was calculated based on the concentration of Al or O on the surface:

$$h = \frac{M_{Al_2O_3} C_{Al_2O_3}}{\rho_{Al_2O_3}}, \tag{22}$$

where $M_{Al_2O_3}$ and $\rho_{Al_2O_3}$ are the molecular mass and density of the alumina, respectively, while $C_{Al_2O_3}$ denotes the bulk concentration of alumina film. The concentration of Al_2O_3 can be obtained from the concentration of oxygen in the OH and MMAOH species, or the aluminum in the DMA and MMA species [14]. In the temperature range used in this study, the Al_2O_3 thin film was amorphous with a density between 3.5 and 3.7 g/cm^3 [25,26]. Simulations were conducted within this range, but no significant difference in thickness was observed, and this parameter was considered constant.

3.2. Partial Pressure Calculation

During the ALD cycle, the total pressure within the reactor was not constant. The precursors, TMA and H_2O, were introduced into the chamber during their respective pulses and were consumed by surface reactions, producing CH_4 in the gas phase. Nitrogen (N_2) was used for purging and to maintain constant pressure. The pumping system evacuated all gases from the reactor. The partial pressure, P_i, of TMA, H_2O, CH_4, and N_2 within the system was determined assuming ideal gas behavior:

$$P_i = \frac{N_i RT}{V}. \quad (23)$$

The number of moles, N_i, was derived from the balance equation between the gas supply and consumption rates:

$$\frac{dN_i}{dt} = Q_{mol,i} \pm R_{r,i} A_s - R_{pump,i} - R_{purge,i}, \quad (24)$$

where $Q_{mol,i}$ is the molar flow rate for species i entering the system, in $mol.s^{-1}$. The first term applied to nitrogen during the entire cycle and to TMA and H_2O during their pulses. The second term represented precursor gas consumption of precursor gases due to the reaction with the surface area A_s, occurring only during the precursor pulse and in the next purge (Equation (19)). CH_4, as a product of surface reaction, made this term positive for a gas that is calculated by the reactions that produce it (Equations (7)–(10)). The third term, describing gas consumption by the pumping system, was considered for all gas species throughout the cycle. The gas pumping rate was defined as:

$$R_{pump,i} = k_{bomb} f_{mol,i}, \quad (25)$$

where $f_{mol,i}$ is the molar fraction of species i, $f_{mol,i} = N_i / N_{mol,T}$, and k_{bomb} is the pumping constant in $mol.s^{-1}$ [30].

$$k_{bomb} = \frac{N_{mol,T} V_B}{V}. \quad (26)$$

Here, $N_{mol,T}$ is the total number of moles of gas in the chamber volume V, and V_B is the pumping velocity, in $m^3.s^{-1}$. The fourth term represented the removal of gas through purging, as in the system employed in this study, N_2 flowed through the reactor continuously throughout the entire ALD cycle. The purge contributed to the removal of the remaining gas molecules in the system. This term was considered for TMA, H_2O, and CH_4. The loss rate due to purge was [31]:

$$R_{purge,i} = \frac{Q_{purge}}{V} N_i, \quad (27)$$

where Q_{purge} is the flow rate of the purge gas N_2, in $m^3.s^{-1}$.

3.3. Input Parameters for ALD Modelling and Simulations

To evaluate the impact of precursor flow on film growth, we employed the previously described model to simulate the atomic layer deposition (ALD) process. The simulations were conducted using the parameters for Al_2O_3 thin film growth, as detailed in Section 4. The model assumed that the precursor reacted with the surface only during its pulse and the subsequent purge phase. This approach was based on the system's geometry, considering both the volume and surface area of the reactor. The precursor flow rate, an essential input in the model, aligned with the values detailed in Section 4.2.

Table 1 lists the input parameters used in the simulations. In our model, we assumed that the initial sticking coefficient for water was the same for DMA, MMA, and MMAOH. The intial sticking coefficient for TMA on OH was determined by fitting the model to the observed the film thickness, a method also employed by Gakis's model, where both

initial sticking coefficients were used as fitting parameters. The fitting was based on film thickness data. For TMA, we tested the range suggested by Arts et al. (2019), which was (0.5–2) $\times 10^{-3}$, and found that the optimal value for our model was 1×10^{-3}. Regarding H_2O, the literature indicates that the initial sticking coefficient ranges from (0.8–2) $\times 10^{-4}$ at a substrate temperature of 220 °C, decreasing to (1.5–2.3) $\times 10^{-5}$ at 150 °C [32]. However, for our model, the best value was determined to be 3×10^{-3}, which was higher than typically reported in the literature.

Table 1. Input parameters for the ALD Al_2O_3 process simulation.

Parameter	Symbol	Value	Reference
Adsorption activation energy	$E_{ads,i}$	TMA: 0 H_2O: 0	[18]
Desorption activation energy	$E_{des,i}$	TMA: 1.13 eV H_2O on DMA and MMA: 0.64 eV H_2O on MMAOH: 1.13 eV	
Reaction activation energy	$E_{r,i}$	TMA: 0.35 eV H_2O on DMA and MMA: 0.44 eV H_2O on MMAOH: 0.67 eV	
Initial sticking coefficient	$s_{0,i}$	TMA: 0.001 H_2O: 0.003	Fitted
Bulk concentration of alumina	$\rho_{Al_2O_3}$	3500 $kg.m^{-3}$	[33]
Pumping speed	V_B	28 m^3h^{-1}	-
Reactor geometry		Diameter: 15.0 cm Height: 1.5 cm	-
Temperature	T	150 °C (423 K) 200 °C (473 K)	-
ALD cycle		TMA and H_2O pulses: 90 ms Purges: 2 s Cycles: 1000	-
N_2 flow rate	Q_{purge}	150 sccm	-

The activation energy for the adsorption of TMA and water was considered negligible, implying that there was no energy barrier for these molecules to adsorb onto the surface. The activation energies for desorption and adsorption were based on the findings of Weckman and Laasonen [18]. It was also assumed that the activation energies for reaction and desorption of H_2O on DMA and MMA were identical. This assumption aligned with the considerations made in Gakis's model [14].

4. Experimental

The experimental phase involved the deposition of Al_2O_3 thin films through ALD, and determining the precursors' flow rates.

4.1. Al_2O_3 Thin Film Growth

Al_2O_3 thin films were deposited using a cross-flow thermal ALD reactor at temperatures of 150 °C and 200 °C. Trimethylaluminum (97%, Sigma-Aldrich, São Paulo, Brazil) and deionized (DI) water were used as the metallic and oxidant precursors, respectively. Nitrogen (N_2, White Martins, 99.999%) was used both as a purge gas and as a carrier for the precursors, maintained at 150 sccm throughout the deposition process. The pulsing of TMA and DI water was controlled using solenoid valves, while their flow rates were regulated by Swagelok micrometer needle valves (model SS-4BMRW). Each ALD cycle comprised a TMA pulse (90 ms), an N_2 purge (2000 ms, 150 sccm), an H_2O pulse (90 ms), and a subsequent N_2 purge (2000 ms, 150 sccm). The pulse duration was consistent for both precursors,

with the flow rate being the sole variable parameter. The thin films were grown on p-type <100> Si substrates (University Wafer Inc., South Boston, MA, USA) over 1000 cycles. Film thickness measurements were performed using reflectance spectroscopy (NanoCalc Thin Film Reflectometry System, Ocean Optics). Chemical bonding analysis of the samples was conducted using an ATR-FTIR PerkinElmer 400 IR spectrometer (PerkinElmer, São Paulo, Brazil) at a resolution of 2 cm^{-1}.

4.2. Precursor Flow Rate Measurement

Due to the challenges associated with directly measuring precursor flow in the ALD system, the gas flow was estimated using the system's capacitance. The flow rate through any given section is calculated as [34]:

$$Q = C(p_1 - p_2), \tag{28}$$

where p_1 and p_2 represent the pressures at the inlet and outlet ends of the system, respectively. The proportionality factor, denoted as C, represents the conductance. In vacuum conditions, C depends on both the pressure and the geometry of the system. Specifically, for laminar flow conditions, applicable when $d.\overline{p} > 6.10^{-1}$mbar.cm (where d is the pipe diameter and $\overline{p} = \frac{p_1+p_2}{2}$ is the mean pressure), the capacitance, expressed in $l.s^{-1}$, is given by [34]:

$$C = 135\frac{d^4}{l}\overline{p} \tag{29}$$

Here, l is the distance between the inlet and outlet of the system. In our setup, l = 78 cm and d = 0.4 cm.

In this study, the partial pressures p_1 and p_2 for the precursors TMA and H_2O were determined from gas pressure sensors positioned at the precursor inlet line and at the entrance of the reactor. These measurements were conducted using a Pirani capacitance diaphragm gauge (PCG-750 Agilent). The micrometer valve adjustments ranged from 0.5 to 2.0 turns. Measurements were performed during the same ALD cycle used in the depositions, but with only one precursor entering the system, while N_2 and the other precursor were disconnected. Figures 3 and 4 illustrate the pressures in the inlet line and at the reactor's entrance for H_2O and TMA, respectively.

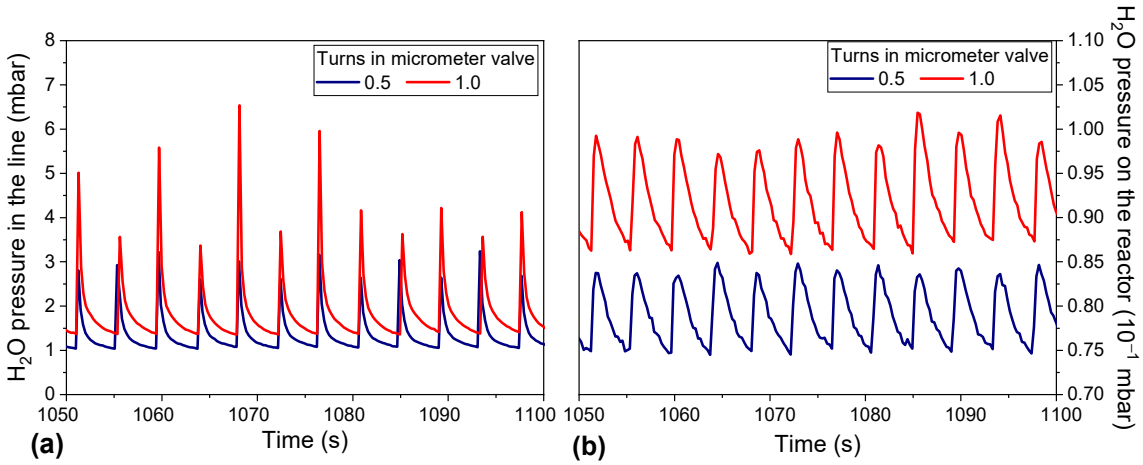

Figure 3. Measured H_2O pressure in precursor line (**a**) and the reactor (**b**) for 0.5 and 1.0 turns of the precursor micrometer valve.

Upon initiation of the precursor pulse, the pressure in both precursor line and the reactor entrance rapidly increased, reaching a peak (as shown in Figures 3 and 4). During the pulse, the precursor was evacuated from the reactor by the pumping system, resulting in a pressure drop. The precursor pressure was consistently higher in the inlet line than in the reactor for both precursors. The peaks reflected the amount of precursor supplied

during a pulse. The pressures p_1 and p_2 were calculated as the average of 100 peaks of the signals measured in the precursor line and in the reactor, respectively, to account for oscillations in the pressure values (Figures 3 and 4). Figure 5 presents p_1 and p_2 for TMA and water. For both precursors, increasing the turns on the micrometer valve raised the pressure in the precursor line and reactor, as expected, with a near-linear relationship to the microvalve turns. For TMA, obtaining pressure in the line for 0.25, 0.5, and 0.75 turns was challenging due to the low sensitivity of the gas pressure sensor. For these cases, the pressure p1 was estimated through the proportion between p_1 and p_2 for them and for 2.0 turns in the micrometer valve.

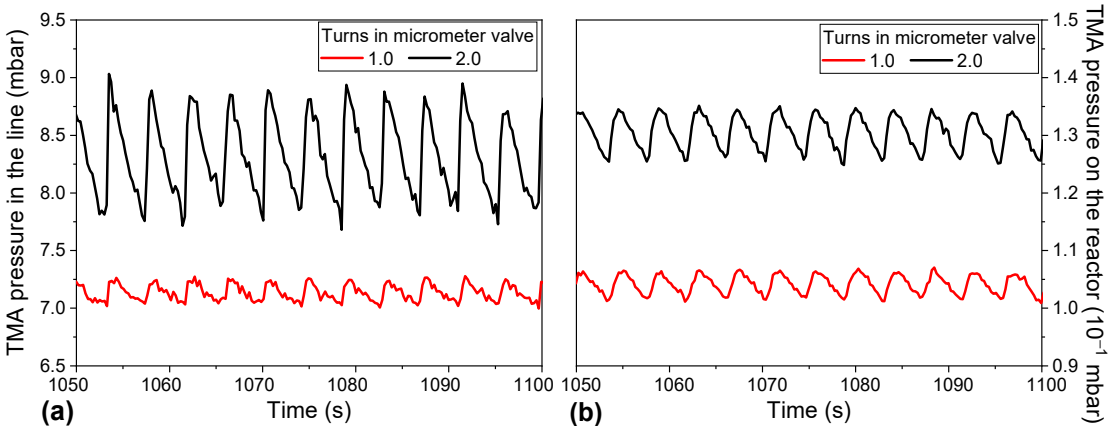

Figure 4. Measured TMA pressure in precursor line (**a**) and the reactor (**b**) for 1.0 and 2.0 turns of the precursor micrometer valve.

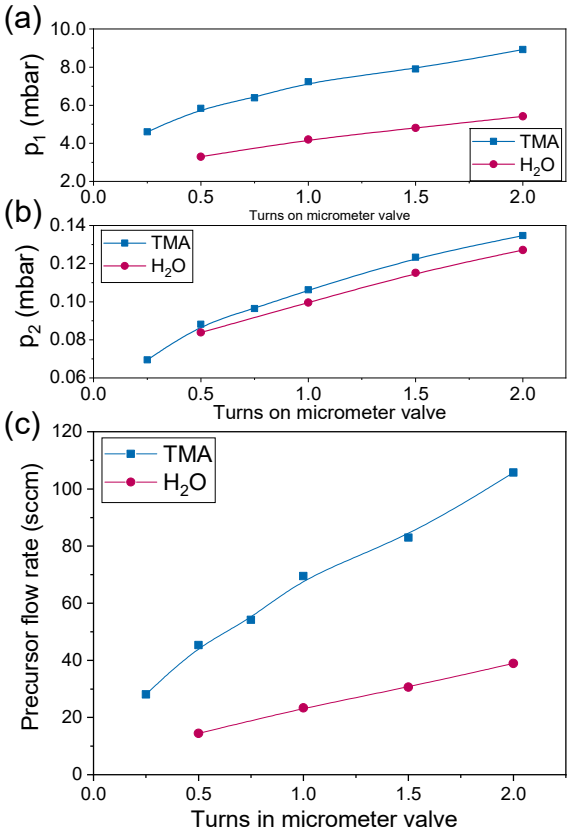

Figure 5. Total pressure in the inlet line (p_1) (**a**) and at the entrance of the reactor (p_2) (**b**), and the calculated precursors flow rate (**c**) for TMA and H_2O as a function of turns in the micrometer needle valve.

Figure 5b shows the calculated precursors flow rate from Equation (28). For a given micrometer valve turn, the flow rate of TMA was higher than that of water, which was attributed to the higher p_1 pressure for TMA. Pressure p_2 was comparable for both precursors. It was assumed that the precursor flow in the line connecting the precursor canister to the reactor was the same as within the reactor.

5. Results and Discussion

5.1. Film Thickness Dependence with TMA Flow Rate and Temperature

Figure 6 illustrates the deposition profiles of Al_2O_3 thin films at deposition temperatures of 150 °C and 200 °C, highlighting the effect of micrometer valve (or precursor flow rate) adjustments on film thickness. At the onset of deposition, the thinnest films corresponded to the smallest TMA micrometer valve opening of 0.25 turns, suggesting a limited supply of TMA precursor for surface reactions. As the valve opening increased, a rise in precursor flow and subsequent film thickness was noted. Notably, at 150 °C, film thickness growth exhibited saturation beyond a valve opening of 1.0 turn, while at 200 °C, a peak and subsequent slight reduction in thickness was recorded beyond the same valve opening. This phenomenon could be indicative of dynamic equilibrium between adsorption and desorption processes at elevated temperatures. Additionally, the films deposited at 150 °C demonstrated consistently greater thickness compared to those at 200 °C under identical TMA flow conditions, possibly due to reduced thermal desorption at the lower temperature.

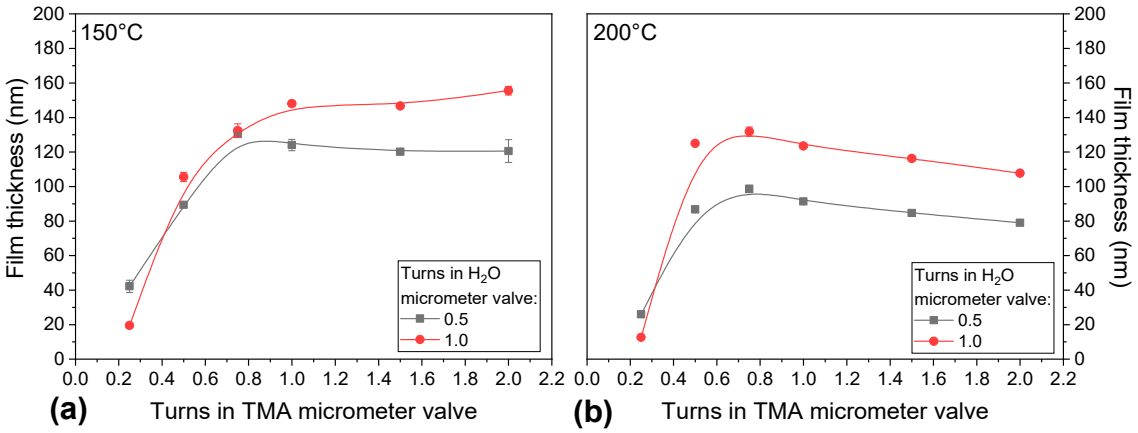

Figure 6. Film thickness at 150 °C (**a**) and 200 °C (**b**) as function of turns in the TMA and H_2O micrometer valves.

This reduction in film thickness with increasing temperature has been reported in the literature. Groner et al. observed that above 125 °C, the GPC decreased, attributed to an increased desorption rate and enhanced film density [35]. At 150 °C, they found the GPC to be approximately 1.3 Å/cycle, which lies within the range of saturation points observed in the current study for two different water flow rates, namely around 1.22 Å/cycle and 1.48 Å/cycle for 0.5 and 1.0 turns on the micrometer valve for H_2O, respectively (Figure 6a). Ott et al. and Cheng et al. observed a similar trend, where the GPC began to level off at temperatures above 170 °C, with a GPC of around 1.05 Å/cycle at both 150 °C and 200 °C [33,36].

An increase in the H_2O valve opening led to thicker films at both deposition temperatures, underscoring the essential role of water vapour as a key reactant. Kuse et al. studied the effects of precursor concentration and also observed an increase in the film thickness with an increase in the concentration of H_2O or TMA [26]. Matero et al. (2000) investigated the impact of water dosage on oxide deposition. Their findings revealed that the GPC initially increased rapidly with rising H_2O dosage, and then reached saturation [12]. This suggests that beyond a certain point, further enhancement of the H_2O flow

rate does not significantly influence film thickness, akin to the trend seen with TMA flow rate adjustments.

To further elucidate the deposition process, a surface kinetic model was applied to simulate the growth of thin films, utilizing precursor flow rates derived from micrometer valve settings for both TMA and H_2O as input parameters, as shown in Figure 5b. Figure 7 compares these calculated flow rates with both experimental and simulated film thickness outcomes. The H_2O flow rates at 14.5 sccm and 23.5 sccm corresponded to half and full turns of the H_2O micrometer valve, respectively. The simulations initially showed an increase in film thickness with rising TMA flow rates, then reaching a plateau that reflected the self-limiting nature of the ALD process. However, the experimental data not only showcase a similar trend of thickness augmentation with increased TMA flow, but also a pronounced decrease in thickness at higher TMA rates. As the model did not account for certain phenomena, such as the spatial variation in parameters, the interactions of adsorbed species, and diffusion on the surface, it is reasonable to expect that the model may have exhibited some discrepancies compared to experimental results. However, since our objective was to construct a simple model to simulate the process quickly, such discrepancies were anticipated in the model results.

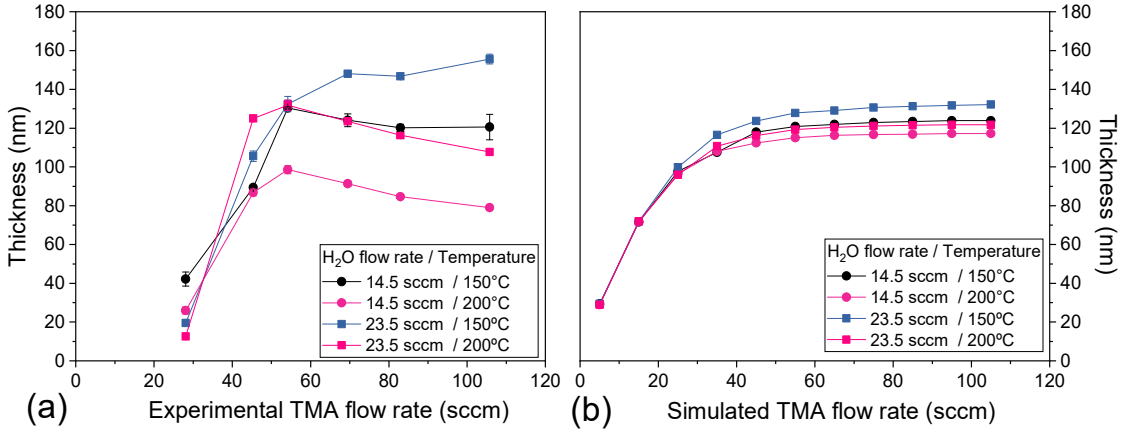

Figure 7. Experimental (**a**) and simulated (**b**) thickness of Al_2O_3 films as a function of TMA gas flow rate. The H_2O flow rates of 14.5 sccm and 23.5 sccm correspond to 0.5 and 1.0 turns on the micrometer valve, respectively.

The decrease in thickness after 60 sccm was only observed at 200 °C, indicating that its effect was associated with the substrate temperature. As the temperature rose, desorption from the surface increased. When the TMA flow rate exceeded 60 sccm, the substrate surface may have become overcrowded with precursor molecules. This overcrowding can enhance the likelihood of desorption events, where adsorbed species, including both TMA and any intermediates formed during the reaction, are ejected back into the gas phase. Such increased desorption rates reduce the amount of material available to contribute to film growth, resulting in a thinner film. However, this effect could not be observed in the simulation. The desorption rate is a function of the activation energy obtained from the literature. The existing literature does not account for the consequences of a large quantity of precursor adsorption on the surface. To further validate and address these observations, it is suggested that future research efforts refine the simulation model by incorporating more detailed mechanisms of desorption.

The simulations also reflected the experimental trend of reduced film growth at the higher temperature of 200 °C. Nonetheless, the absolute film thicknesses under certain simulated conditions diverged from the experimental data. These discrepancies were likely due to the model's simplifications, such as assuming a perfectly stoichiometric reaction and neglecting certain chemical vapour deposition (CVD) effects, which may not have fully captured the complexities of the actual process. Despite these differences, the

consistent qualitative effects of precursor flow rate and deposition temperature on film growth observed in both the simulations and experiments underscore the model's value in providing insights into the surface kinetics of ALD Al_2O_3 thin film.

The dependency of film thickness on temperature exhibited variation with the increase in precursor flow rates, as demonstrated in Figure 7b. The influence of temperature on film thickness was minimal at TMA flow rates up to 30 sccm. This observation is corroborated by Figure 8, which indicates that at a TMA flow rate of 5 sccm, the film thickness remained relatively consistent across a broad temperature range. However, as the flow rates of TMA and H_2O were augmented, an increase in film thickness was observed, although this increase was not uniform across all temperatures. At the lower temperature range, the increment in precursor flow exerted a more substantial effect, with film thickness not reaching saturation until a TMA flow of 105 sccm was applied, aligning with results observed at 150 °C. In contrast, an increase in temperature resulted in a reduction in film thickness, more so under elevated precursor flow conditions. This behavior can be elucidated by considering the rate constants for reaction and desorption, along with the temperature-dependent concentration of OH sites.

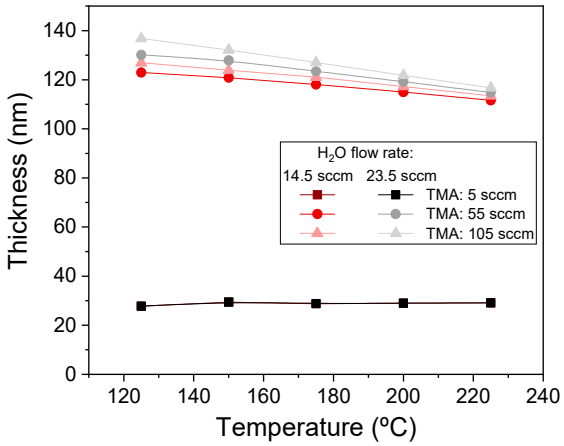

Figure 8. Variation in Al_2O_3 film thickness with deposition temperature at different TMA and H_2O flow rates.

Figure 9 depicts the temperature-dependent rate constants for TMA desorption and surface reactions on OH sites, as well as for H_2O interactions with DMA, MMA, and MMAOH, as defined by Equation (20). It is noted that the rate constants for both surface reactions and desorption processes increased with temperature, which can be ascribed to the additional thermal energy that enabled the precursors to overcome activation barriers. However, the desorption processes, particularly for TMA on OH and H_2O on MMAOH sites, exhibited a more pronounced increase in rate constants at elevated temperatures compared to the other reaction rate constants. This greater increase was attributed to the higher activation energies associated with desorption. Consequently, the increase in the desorption contributed to decreased film thickness at elevated temperatures. In the Gakis model, different activation energies were applied, suggesting that water was more likely to desorb than react due to a lower energy barrier for desorption compared to the irreversible surface reaction [14,27]. This affected the temperature dependence of film thickness, which notably increased from 150 °C to 200 °C.

Furthermore, the decrease in film thickness with rising temperature can also be linked to the reduced concentration of available reactive sites on the surface, a factor which was temperature-dependent, as described by Equation (12) [29,37,38]. This decrease in available sites resulted in lower surface concentrations of oxygen and aluminium, further affecting the film growth. Therefore, the interplay between the enhanced desorption rates and the diminishing concentration of reactive sites with temperature contributed to the observed thinning of films at higher temperatures.

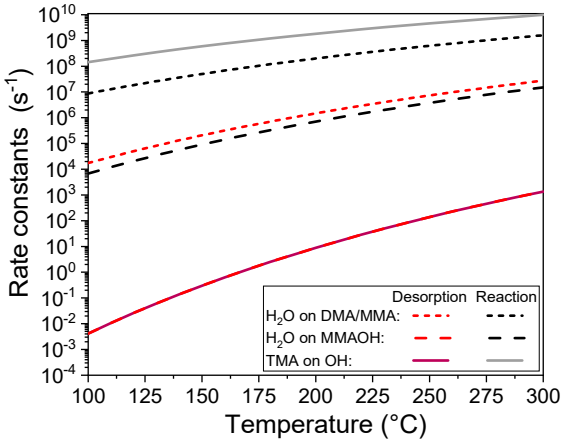

Figure 9. Temperature-dependent rate constants for TMA desorption and surface reactions on OH sites, and H_2O interactions with DMA, MMA, and MMAOH.

5.2. Surface Kinetic

Figure 10 traces the dynamic changes in surface coverage fractions for DMA, MMA, OH, and MMAOH during the ALD process at 200 °C, with a water flow rate of 23.5 sccm and varying TMA flow rates. The simulation initiated with a TMA pulse, leading to a reaction with OH groups on the substrate surface, which reduced the OH coverage while generating MMA and DMA species, as shown in Figure 11.The prevalence of MMA in the surface coverage, compared to DMA, was attributed to its stoichiometry, which involves binding to two OH sites per molecule (as shown in Figure 1).

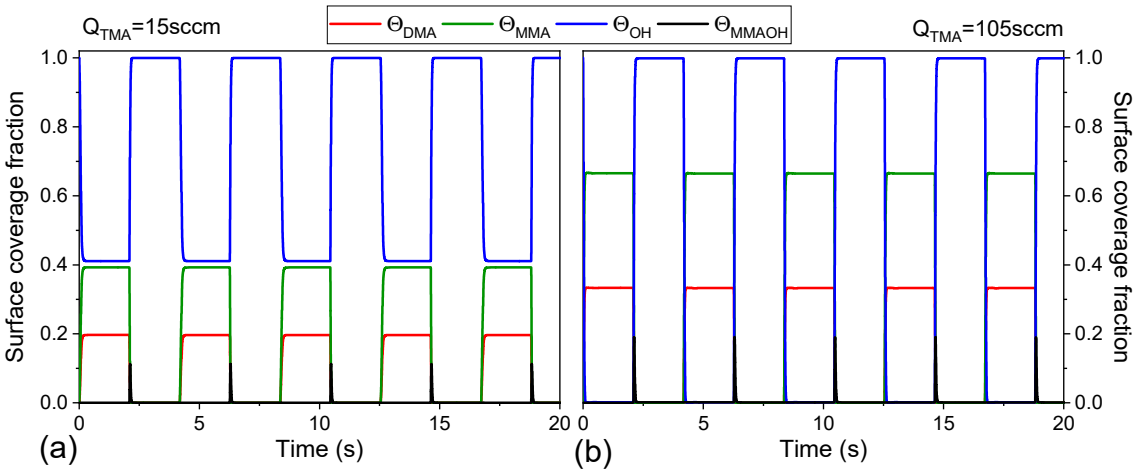

Figure 10. Temporal evolution of surface coverage fractions for DMA, MMA, OH, and MMAOH during an ALD cycle at 200 °C with 23.5 sccm of H_2O, and TMA flow rates of 15 sccm (**a**) and 105 sccm (**b**).

The subsequent purge phase may have allowed any remaining TMA within the reactor to continue reacting with available surface sites; however, this reaction quickly diminished as the precursor was purged from the system (Figure 12), resulting in the stabilization of surface coverage fractions, as corroborated by Travis and Adomaitis [39]. When the H_2O pulse was introduced, it reactivated the surface chemistry: OH groups were replenished through reactions with DMA and MMA, reducing their surface coverage while increasing θ_{OH}. Concurrently, MMAOH species were generated via the interaction of water with DMA, which further reacted to regenerate OH groups.

Each new TMA pulse restarted the cycle, interacting with the replenished OH sites and perpetuating the sequence of surface reactions. This cyclical nature of the ALD process is crucial for controlling film growth and composition, as it methodically alternates between

the addition of chemical species and the restoration of reactive sites, ensuring consistent surface kinetics during deposition.

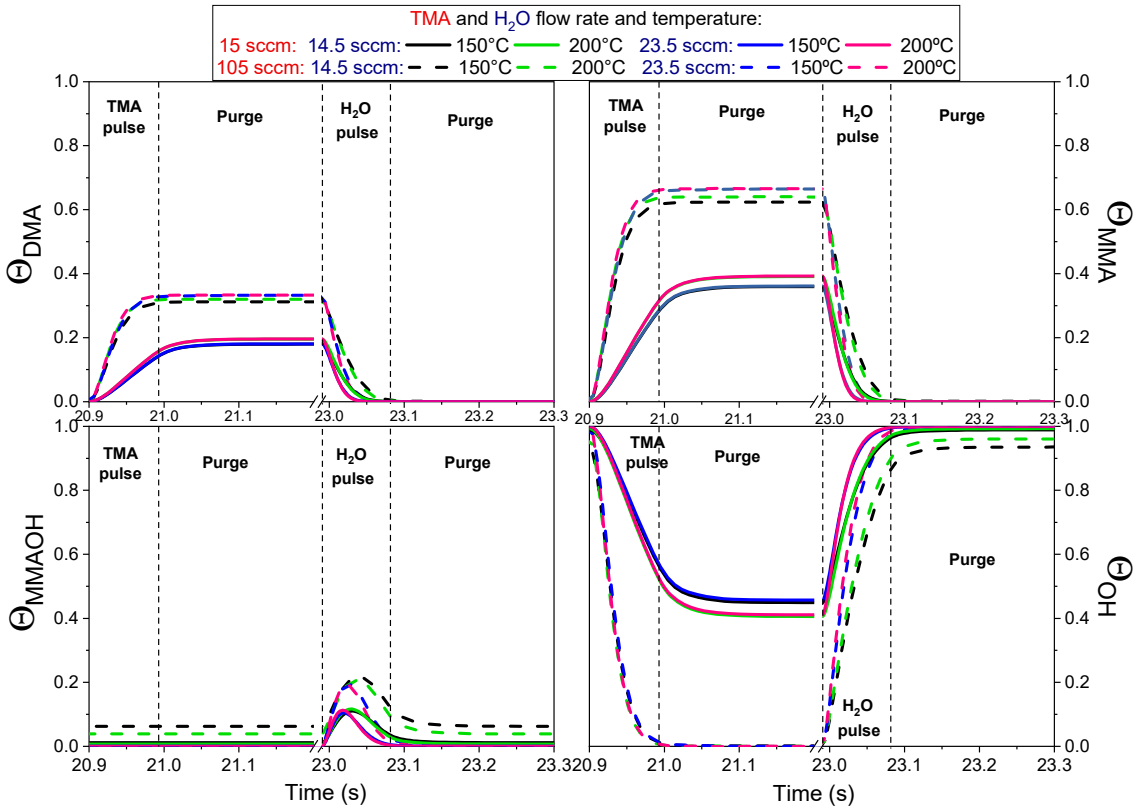

Figure 11. Surface coverage fraction of DMA, MMA, MMAOH, and OH for 15 sccm and 105 sccm of TMA and for 14.5 sccm and 23.5 sccm of water at 150 °C and 200 °C.

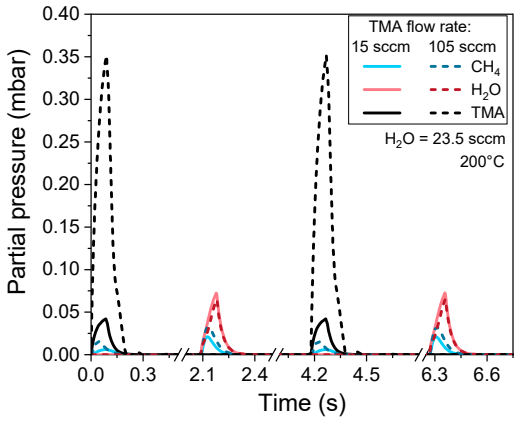

Figure 12. Variations in partial pressure for TMA, H_2O, and CH_4 at 200 °C with water flow rate at 23.5 sccm, and TMA flow rates of 15 sccm and 105 sccm.

Figure 11 presents the surface coverage fraction during a single ALD pulse. This is plotted for the sixth pulse because the θ_{MMAOH} typically takes around four cycles to stabilize, as referenced in [14]. The surface species dynamics were similar across different TMA flow rates, yet the coverage ratios vary. At a lower TMA flow rate of 15 sccm, around 60% of the OH sites reacted with the precursor, forming 20% DMA and 40% MMA. At a higher flow rate of 105 sccm, almost all of the OH sites were consumed, yielding MMA and DMA. This figure demonstrates the surface coverage fractions of DMA, MMA, MMAOH,

and OH throughout an ALD cycle, reflecting the effects of TMA flow rates, water flow rates, and process temperature variations.

During the TMA pulse, for all conditions, θ_{DMA} and θ_{MMA} increased on the surface, reducing θ_{OH} and reaching saturation during the purge. The remaining precursor in the reactor continued reacting with the surface. Figure 12 illustrates the TMA and H_2O partial pressures during one ALD cycle. When the pulse ended and the precursor input stopped, the pressure began to decrease rapidly, reaching zero in about 300 ms, and reactions continued until the precursor was fully purged.

An increase in TMA flow rate resulted in higher partial pressure of this precursor during pulses (Figure 13), leading to a rise in TMA flux to the surface (Equation (17)) and an increase in adsorption rate (Equation (15)). More TMA adsorption amplified both reaction and desorption rates, as shown in Figure 13. The reaction rate was higher than the desorption rate, consuming more OH sites, as demonstrated in Figure 11. At a flow rate of 105 sccm, the consumption of OH sites was nearly complete before the pulse concluded, contributing to an increase in film thickness. However, there was a saturation point in film growth due to the limited number of active sites for reaction on surface, as depicted in Figure 7 and also presented by Travis and Adomaitis [40]. The model suggested a finite number of activated sites for reaction; beyond this limit, no additional reactions could proceed, a finding echoed by Poodt et al. (2013), who modeled the growth per cycle as a function of TMA and water partial pressures [41]. For both precursors, saturation in the GPC was observed.

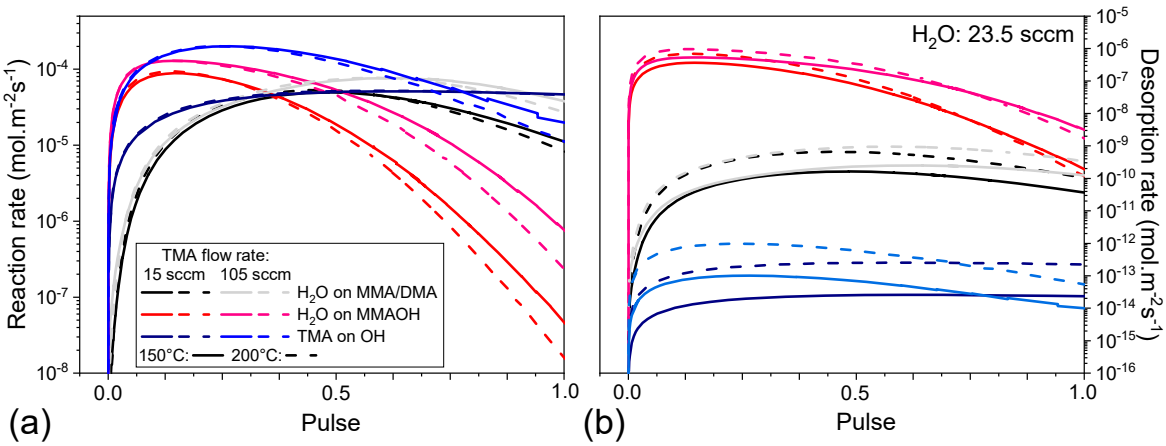

Figure 13. TMA and H_2O reaction rate (**a**) and desorption rate (**b**) during one pulse at 150 °C (solid line) and 200 °C (dashed line) for 15 sccm and 105 sccm of TMA.

For TMA flow rates of 15 sccm, the θ_{OH} values became higher at 200 °C than at 150 °C during the purge after the pulse. The reaction rate was consistent for both temperatures (see Figure 13a), although the desorption of TMA adsorbed on OH was higher at 200 °C (see Figure 13b). Consequently, during the purge, the TMA pressure decreased in the reactor, reducing the reaction. However, desorption still occurred, leading to a decrease in MMA and DMA at 200 °C compared to 150 °C.

During the water pulse, water reacted with the methyl radicals on the surface, forming MMAOH. The fraction of MMAOH increased when the water pulse began, but decreased as it reacted with water, forming OH (Figure 12). Increasing the TMA flow rate enhanced both the reaction and desorption rates of water on DMA and MMA along the oxidant pulse (Figure 13). This is because a higher fraction of these species was present during the TMA pulse, leading to a more pronounced formation of MMAOH and OH in the water pulse since the reaction rate was higher than the desorption rate.

A decrease in water flow rate led to a reduction in reactions due to the decreased rate constant (Figure 13), leaving MMAOH partially unreacted during the pulse (Figure 11). This effect was more noticeable at a TMA flow rate of 105 sccm. When the available H_2O

molecules for surface reactions were consumed, MMAOH levels stabilized, affecting the proportion of OH produced during the water pulse. For 105 sccm of TMA and 14.5 sccm of H_2O, θ_{MAAOH} was higher for 150 °C than 200 °C when the water reaction stopped. The increase in temperature decreased the reaction rate of water with MMAOH during the pulse (Figure 13a). The difference in the θ_{MAAOH} due to water flow rate and temperature affected the fractions of the other species (Figure 11) during the deposition. Consequently, in the subsequent TMA pulse, fewer OH sites were available for reaction, reducing the coverage fractions of MMA and DMA.

During the pulse, the precursor's entry into the reactor caused an increase in partial pressure. Figure 13 displays the partial pressures in the reactor of H_2O, TMA, and CH_4. The partial pressure of TMA exceeded that of water and methane. This observation was consistent with the dynamic ALD process model developed by Travis and Adomaitis [30].

Surface reactions produced CH_4 in the gas phase, which desorbed from the surface. During the TMA pulse, two CH_4 molecules were produced per DMA and MMA formed, leading to the production of three CH_4 molecules for every two TMA molecules. In the H_2O pulse, one CH_4 molecule was formed in the reaction with MMA, and two more were produced in the reaction with DMA. This maintained the stoichiometry of the alumina formation reaction (Equation (1)). The CH_4 partial pressure peaks during the oxidizing pulse were higher than in the TMA pulse (Figure 12), indicating that more reaction occurred during this pulse until surface saturation was reached. This phenomenon has also been experimentally verified by Chaves et al. [42] and reflected in simulations by Travis and Adomaitis [30]. In addition, an increase in the TMA flow rate increased the methane partial pressure due to associated increases in the reaction rates.

5.3. FTIR Analyses

Figure 14 presents the FTIR spectral analysis of Al_2O_3 films deposited via ALD at different TMA flow rates and temperatures, highlighting the nuances of the ALD process and the chemical characteristics of the resulting films.

In the FTIR spectra, the broad band from 400 cm^{-1} to 1000 cm^{-1} suggests a variety of Al–O interactions, which is consistent with the presence of both tetrahedral (AlO_4) and octahedral (AlO_6) aluminum sites in the film [43]. The peak at around 516 cm^{-1} is indicative of Al–O vibrations specifically in AlO_6 structures, while the peak at 668 cm^{-1} corresponds to O–Al–O bending vibrations [43,44].

The relative peak intensity for the C–H bending mode being most prominent in the H_2O-based Al_2O_3 film implies that the incorporation of hydrocarbons into the film was significant. The presence of absorption peaks associated with carbon species—such as the C–O stretching vibrations at 1050 cm^{-1} and the symmetric and antisymmetric OCO modes at 1326 and 1609 cm^{-1}—indicates that carbon contaminants from the TMA precursor were indeed present in the film [44]. This is a common issue in ALD, where complete removal of organic precursors can be challenging, particularly at lower deposition temperatures where the desorption rates of the byproducts are reduced.

The remaining carbon in a film can affect the dielectric properties and purity of the Al_2O_3 layer, which can be particularly problematic for electronic applications where high purity and precise control of film composition are required [45].

Interestingly, the observation that some TMA flow rates led to a decrease in C-bond species suggests that there may be a flow rate that optimizes the removal of carbon species, potentially through more effective reactions with H_2O or enhanced desorption at certain conditions. Identifying the optimal TMA flow rate is crucial to minimize carbon contamination and to achieve the desired self-limiting growth characteristic of the ALD process. However, to provide a more comprehensive analysis, future studies should employ techniques such as Rutherford backscattering spectrometry (RBS) and/or X-ray photoelectron spectroscopy (XPS).

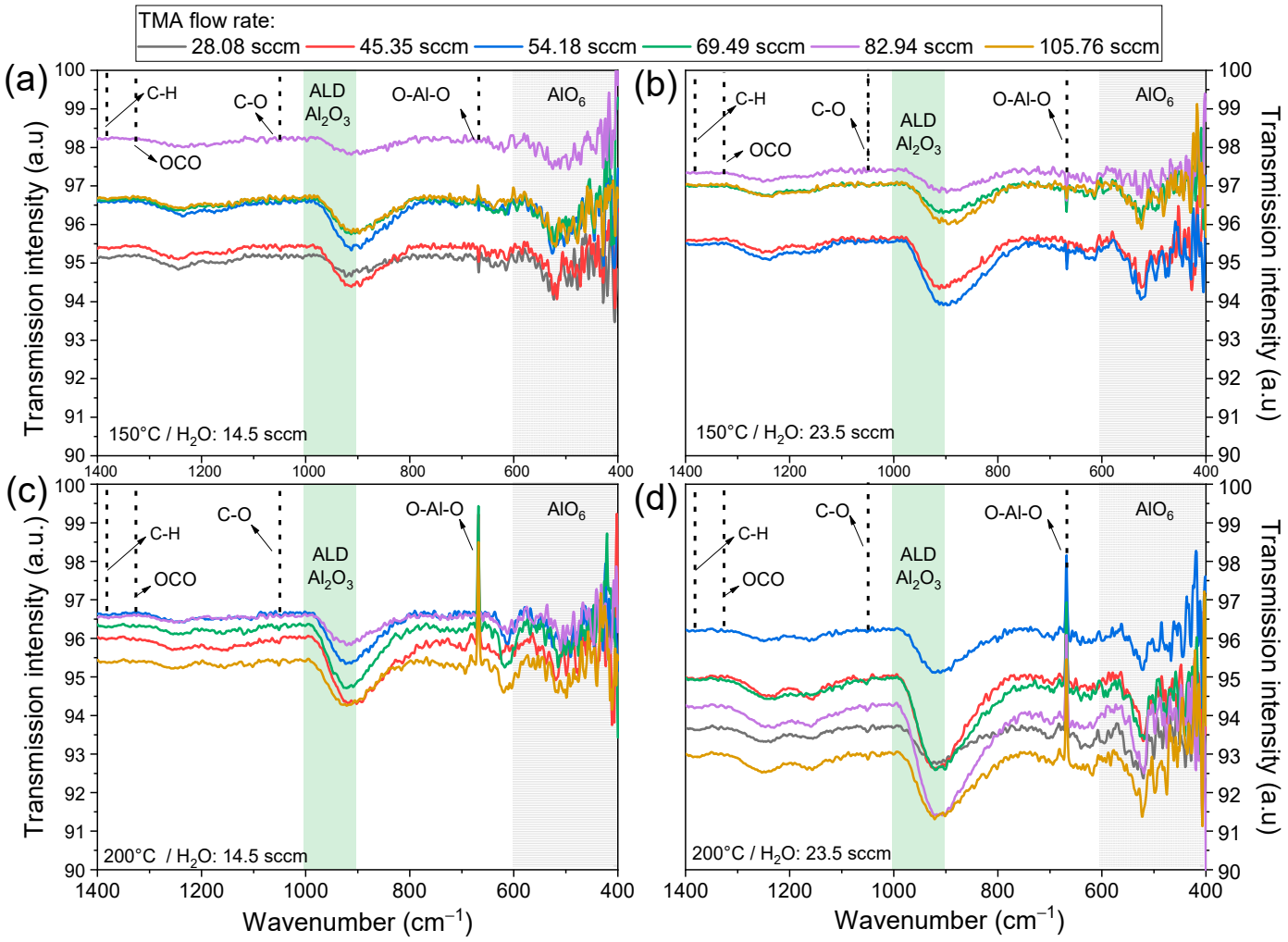

Figure 14. FTIR analyses of the Al_2O_3 film deposited at 150 °C (**a**,**b**) and 200 °C (**c**,**d**), changing the precursors micrometer valve opening.

6. Conclusions

This study explored the impact of TMA and H_2O flow rates on the deposition of Al_2O_3 thin films using atomic layer deposition (ALD), employing both experimental techniques and simulation models. The experiments used TMA and deionized water as precursors at temperatures of 150 °C and 200 °C. Precursor flow rates, determined by system conductance, were integrated into surface kinetic simulations to analyze the film growth mechanisms, utilizing a zero-dimensional model for the kinetic study.

Experimentally, lower TMA flow rates led to the formation of thinner Al_2O_3 films, suggesting a limited availability of TMA for necessary surface reactions. As TMA flow rate increased, a marked increase in film thickness was noted. At 150 °C, film thickness reached saturation; however, at 200 °C, the film thickness initially peaked but then began to decline when TMA flow rates exceeded 60 sccm, highlighting the significant influence of deposition temperature. Higher temperatures generally resulted in thinner films due to accelerated species desorption. Conversely, increased water flow rates consistently produced thicker films, underscoring the crucial role of water vapour in facilitating surface reactions and influencing film growth dynamics.

The simulations aligned with the experimental observations, showing increases and eventual saturation in film thickness at rising TMA flow rates. This saturation was attributed to the limited number of reactive sites available for surface reactions, which became increasingly occupied as the TMA flow rate escalated. Notably, after surpassing 60

sccm, a significant decrease in film thickness was observed at 200 °C, demonstrating the intricate interplay between flow rate and deposition dynamics.

An increase in TMA flow profoundly affected the surface chemistry, altering the coverage fractions of species like DMA and MMA, and significantly modifying the partial pressures and reaction rates during deposition. This led to complex changes in film formation dynamics and overall process efficiency. Excessive TMA flow disrupted the balance of reactions on the surface, leading to suboptimal film formation conditions. This underscores the importance of maintaining an optimal flow rate in achieving desired film characteristics without compromising quality.

Further investigations into this phenomenon could involve deeper exploration of the stoichiometric imbalances and gas-phase reactions that become more prominent at higher flow rates. This would provide a more comprehensive understanding of the dynamic changes impacting film growth and quality as TMA flow rates increase beyond the identified threshold.

Additionally, the interplay between deposition temperature and TMA flow rate was identified as a pivotal factor, with higher temperatures resulting in thinner films regardless of the increased TMA flow, due to enhanced desorption rates. FTIR analysis indicated the potential for optimizing TMA flow rates to improve film purity by reducing carbon contaminants.

In conclusion, these findings underscore the critical role of precise control over TMA and H_2O flow rates in the ALD process. Such control is essential for customizing the properties of Al_2O_3 thin films, making them suitable for a variety of advanced applications.

Author Contributions: Conceptualization, J.K. and R.P.; methodology, J.K. and R.P.; software, J.K.; validation, J.K., N.A.N. and R.P.; formal analysis, J.K. and T.V.; investigation, J.K., N.A.N., T.V., A.d.S.S., J.S. and R.P.; resources, M.F. and R.P.; data curation, J.K.; writing—original draft preparation, J.K. and R.P.; writing—review and editing, J.K., M.F., A.d.S.S., J.S. and R.P.; visualization, J.K.; supervision, J.S. and R.P.; project administration, R.P.; funding acquisition, M.F. and R.P. All authors have read and agreed to the published version of the manuscript.

Funding: This research was funded by FAPESP, grant numbers 2018/01265-1 and 2023/02268-2, and CNPq, grant numbers 402981/2022-7, 313482/2021-7, and 405637/2022-5. Júlia Karnopp and Thais Vieira thank Coordenação de Aperfeiçoamento de Pessoal de Nível Superior—CAPES for the doctorate grant (Finance Code 001).

Institutional Review Board Statement: Not applicable.

Informed Consent Statement: Not applicable.

Data Availability Statement: Data available upon request.

Conflicts of Interest: The authors declare no conflicts of interest.

References

1. Greene, J.E. Review Article: Tracing the Recorded History of Thin-Film Sputter Deposition: From the 1800s to 2017. *J. Vac. Sci. Technol. A* **2017**, *35*, 05C204. [CrossRef]
2. Justin Kunene, T.; Kwanda Tartibu, L.; Ukoba, K.; Jen, T.C. Review of Atomic Layer Deposition Process, Application and Modeling Tools. *Mater. Today Proc.* **2022**, *62*, S95–S109. [CrossRef]
3. Puurunen, R.L. Surface Chemistry of Atomic Layer Deposition: A Case Study for the Trimethylaluminum/Water Process. *J. Appl. Phys.* **2005**, *97*, 121301. [CrossRef]
4. Chiappim, W.; Neto, B.B.; Shiotani, M.; Karnopp, J.; Gonçalves, L.; Chaves, J.P.; Sobrinho, A.d.S.; Leitão, J.P.; Fraga, M.; Pessoa, R. Plasma-Assisted Nanofabrication: The Potential and Challenges in Atomic Layer Deposition and Etching. *Nanomaterials* **2022**, *12*, 3497. [CrossRef]
5. Knoops, H.C.M.; Potts, S.E.; Bol, A.A.; Kessels, W.M.M. Atomic Layer Deposition. In *Handbook of Crystal Growth: Thin Films and Epitaxy: Second Edition*; Elsevier B.V.: Amsterdam, The Netherlands, 2015; Volume 3, pp. 1101–1134. ISBN 9780444633057.
6. Vandalon, V.; Kessels, W.M.M. Revisiting the Growth Mechanism of Atomic Layer Deposition of Al_2O_3: A Vibrational Sum-Frequency Generation Study. *J. Vac. Sci. Technol. A* **2017**, *35*, 05C313. [CrossRef]
7. Dias, V.; Maciel, H.; Fraga, M.; Lobo, A.O.; Pessoa, R.; Marciano, F.R. Atomic Layer Deposited TiO_2 and Al_2O_3 Thin Films as Coatings for Aluminum Food Packaging Application. *Materials* **2019**, *12*, 682. [CrossRef] [PubMed]

8. Jinesh, K.B.; van Hemmen, J.L.; van de Sanden, M.C.M.; Roozeboom, F.; Klootwijk, J.H.; Besling, W.F.A.; Kessels, W.M.M. Dielectric Properties of Thermal and Plasma-Assisted Atomic Layer Deposited Al_2O_3 Thin Films. *J. Electrochem. Soc.* **2011**, *158*, G21. [CrossRef]
9. Daubert, J.S.; Hill, G.T.; Gotsch, H.N.; Gremaud, A.P.; Ovental, J.S.; Williams, P.S.; Oldham, C.J.; Parsons, G.N. Corrosion Protection of Copper Using Al_2O_3, TiO_2, ZnO, HfO_2, and ZrO_2 Atomic Layer Deposition. *ACS Appl. Mater. Interfaces* **2017**, *9*, 4192–4201. [CrossRef] [PubMed]
10. Barbos, C.; Blanc-Pelissier, D.; Fave, A.; Botella, C.; Regreny, P.; Grenet, G.; Blanquet, E.; Crisci, A.; Lemiti, M. Al_2O_3 Thin Films Deposited by Thermal Atomic Layer Deposition: Characterization for Photovoltaic Applications. *Thin Solid Films* **2016**, *617*, 108–113. [CrossRef]
11. Ballestero, M.; Dória, A.C.O.C.; Pessoa, R.S.; Rodrigues, B.V.M. Enhancing Microbiostatic Properties of Silicone Catheters with Al_2O_3 Coatings Deposited by Atomic Layer Deposition. *Mater. Lett.* **2023**, *344*, 2–6. [CrossRef]
12. Matero, R.; Rahtu, A.; Ritala, M.; Leskelä, M.; Sajavaara, T. Effect of Water Dose on the Atomic Layer Deposition Rate of Oxide Thin Films. *Thin Solid Films* **2000**, *368*, 1–7. [CrossRef]
13. Chiappim, W.; Testoni, G.E.; de Lima, J.S.B.; Medeiros, H.S.; Pessoa, R.S.; Grigorov, K.G.; Vieira, L.; Maciel, H.S. Effect of Process Temperature and Reaction Cycle Number on Atomic Layer Deposition of TiO_2 Thin Films Using $TiCl_4$ and H_2O Precursors: Correlation Between Material Properties and Process Environment. *Braz. J. Phys.* **2016**, *46*, 56–69. [CrossRef]
14. Gakis, G.P.; Vergnes, H.; Scheid, E.; Vahlas, C.; Boudouvis, A.G.; Caussat, B. Detailed Investigation of the Surface Mechanisms and Their Interplay with Transport Phenomena in Alumina Atomic Layer Deposition from TMA and Water. *Chem. Eng. Sci.* **2019**, *195*, 399–412. [CrossRef]
15. Lim, J.-W.; Park, H.-S.; Kang, S.-W. Kinetic Modeling of Film Growth Rate in Atomic Layer Deposition. *J. Electrochem. Soc.* **2001**, *148*, C403. [CrossRef]
16. Guerra-Nuñez, C.; Döbeli, M.; Michler, J.; Utke, I. Reaction and Growth Mechanisms in Al_2O_3 deposited via Atomic Layer Deposition: Elucidating the Hydrogen Source. *Chem. Mater.* **2017**, *29*, 8690–8703. [CrossRef]
17. Pan, D. Density Functional Theory (DFT)-Enhanced Computational Fluid Dynamics Modeling of Substrate Movement and Chemical Deposition Process in Spatial Atomic Layer Deposition. *Chem. Eng. Sci.* **2021**, *234*, 116447. [CrossRef]
18. Weckman, T.; Laasonen, K. First Principles Study of the Atomic Layer Deposition of Alumina by TMA-H_2O-Process. *Phys. Chem. Chem. Phys.* **2015**, *17*, 17322–17334. [CrossRef]
19. Kunene, T.J.; Coetzee, R.A.M.; Tartibu, L.; Jen, T.C. Numerical Modeling of Atomic Layer Deposition Supercycles. *Mater. Today Proc.* **2022**, *62*, S30–S39. [CrossRef]
20. Gakis, G.P.; Vergnes, H.; Scheid, E.; Vahlas, C.; Caussat, B.; Boudouvis, A.G. Computational Fluid Dynamics Simulation of the ALD of Alumina from TMA and H_2O in a Commercial Reactor. *Chem. Eng. Res. Des.* **2018**, *132*, 795–811. [CrossRef]
21. Xie, Y.; Pan, D.; Ma, L.; Yuan, C. Optimizing the Process Efficiency of Atomic Layer Deposition of Alumina for Its Sustainability Improvement: A Combined Experimental and Modeling Study. *J. Clean. Prod.* **2016**, *133*, 338–347. [CrossRef]
22. Holmqvist, A.; Törndahl, T.; Magnusson, F.; Zimmermann, U.; Stenström, S. Dynamic Parameter Estimation of Atomic Layer Deposition Kinetics Applied to in Situ Quartz Crystal Microbalance Diagnostics. *Chem. Eng. Sci.* **2014**, *111*, 15–33. [CrossRef]
23. Pan, D.; Jen, T.C.; Yuan, C. Effects of Gap Size, Temperature and Pumping Pressure on the Fluid Dynamics and Chemical Kinetics of in-Line Spatial Atomic Layer Deposition of Al_2O_3. *Int. J. Heat Mass Transf.* **2016**, *96*, 189–198. [CrossRef]
24. Yamamoto, K.; Suzuki, A.; Kagaya, M.; Matsukuma, M.; Moriya, T. Surface Oxidation Model in Plasma Enhanced Atomic Layer Deposition for Silicon Oxide Films Including Various Aminosilane Precursors. *J. Vac. Sci. Technol. A* **2019**, *37*, 020920. [CrossRef]
25. Muneshwar, T.; Cadien, K. Surface Reaction Kinetics in Atomic Layer Deposition: An Analytical Model and Experiments. *J. Appl. Phys.* **2018**, *124*, 095302. [CrossRef]
26. Kuse, R.; Kundu, M.; Yasuda, T.; Miyata, N.; Toriumi, A. Effect of Precursor Concentration in Atomic Layer Deposition of Al_2O_3. *J. Appl. Phys.* **2003**, *94*, 6411–6416. [CrossRef]
27. Widjaja, Y.; Musgrave, C.B. Quantum Chemical Study of the Mechanism of Aluminum Oxide Atomic Layer Deposition. *Appl. Phys. Lett.* **2002**, *80*, 3304–3306. [CrossRef]
28. Dillon, A.C.; Ott, A.W.; Way, J.D.; George, S.M. Surface Chemistry of Al_2O_3 Deposition Using $Al(CH_3)_3$ and H_2O in a Binary Reaction Sequence. *Surf. Sci.* **1995**, *322*, 230–242. [CrossRef]
29. Haukka, S.; Root, A. The Reaction of Hexamethyldisilazane and Subsequent Oxidation of Trimethylsilyl Groups on Silica Studied by Solid-State NMR and FTIR. *J. Physial Chem.* **1994**, *98*, 1695–1703. [CrossRef]
30. Travis, C.D.; Adomaitis, R.A. Dynamic Modeling for the Design and Cyclic Operation of an Atomic Layer Deposition (ALD) Reactor. *Processes* **2013**, *1*, 128–152. [CrossRef]
31. Scialdone, J.J. *Preventing Molecular and Particulate in a Confined Volume*; SPIE: Bellingham, WA, USA, 1999; Volume 2784.
32. Arts, K.; Vandalon, V.; Puurunen, R.L.; Utriainen, M.; Gao, F.; Kessels, W.M.M.; Knoops, H.C.M. Sticking Probabilities of H_2O and $Al(CH_3)_3$ during Atomic Layer Deposition of Al_2O_3 Extracted from Their Impact on Film Conformality. *J. Vac. Sci. Technol. A* **2019**, *37*, 030908. [CrossRef]
33. Ott, A.W.; Klaus, J.W.; Johnson, J.M.; George, S.M. Al_3O_3 Thin Film Growth on Si(100) Using Binary Reaction Sequence Chemistry. *Thin Solid Films* **1997**, *292*, 135–144. [CrossRef]
34. Leybold GmbH. *Fundamentals of Vacuum Technology*; Hermann, A., Alfred, B., Hermann, B., Heinz, D., Karl, G., Wolfgang, J., Walter, M., Hans-Jürgen, M., Hans-Dieter, O., Willi, S., et al., Eds.; Walter Umr.; Leybold: Tokyo, Japan, 2016; ISBN 9783527653898.

35. Groner, M.D.; Fabreguette, F.H.; Elam, J.W.; George, S.M. Low-Temperature Al_2O_3 Atomic Layer Deposition. *Chem. Mater.* **2004**, *16*, 639–645. [CrossRef]
36. Cheng, C.-C.; Chien, C.-H.; Luo, G.-L.; Liu, J.-C.; Kei, C.-C.; Liu, D.-R.; Hsiao, C.-N.; Yang, C.-H.; Chang, C.-Y. Characteristics of Atomic-Layer-Deposited Al_2O_3 High-k Dielectric Films Grown on Ge Substrates. *J. Electrochem. Soc.* **2008**, *155*, G203. [CrossRef]
37. Zhuravlev, L.T. Concentration of Hydroxyl Groups on the Surface of Amorphous Silicas. *Langmuir* **1987**, *3*, 316–318. [CrossRef]
38. Puurunen, R.L. Analysis of Hydroxyl Group Controlled Atomic Layer Deposition of Hafnium Dioxide from Hafnium Tetrachloride and Water. *J. Appl. Phys.* **2004**, *95*, 4777–4786. [CrossRef]
39. Travis, C.D.; Adomaitis, R.A. Modeling Alumina Atomic Layer Deposition Reaction Kinetics during the Trimethylaluminum Exposure. *Theor. Chem. Acc.* **2014**, *133*, 3–11. [CrossRef]
40. Travis, C.D.; Adomaitis, R.A. Modeling ALD Surface Reaction and Process Dynamics Using Absolute Reaction Rate Theory. *Chem. Vap. Depos.* **2013**, *19*, 4–14. [CrossRef]
41. Poodt, P.; van Lieshout, J.; Illiberi, A.; Knaapen, R.; Roozeboom, F.; van Asten, A. On the Kinetics of Spatial Atomic Layer Deposition. *J. Vac. Sci. Technol. A* **2013**, *31*, 01A108. [CrossRef]
42. Chaves, J.; Chiappim, W.; Karnopp, J.; Neto, B.; Leite, D.; da Silva Sobrinho, A.; Pessoa, R. Novel Energetic Co-Reactant for Thermal Oxide Atomic Layer Deposition: The Impact of Plasma-Activated Water on Al_2O_3 Film Growth. *Nanomaterials* **2023**, *13*, 3110. [CrossRef]
43. Gao, M.; Liu, B.; Zhao, P.; Yi, X.; Shen, X.; Xu, Y. Mechanical Strengths and Thermal Properties of Titania-Doped Alumina Aerogels and the Application as High-Temperature Thermal Insulator. *J. Sol-Gel Sci. Technol.* **2019**, *91*, 514–522. [CrossRef]
44. Wang, H.; Liu, Y.; Liu, H.; Chen, Z.; Xiong, P.; Xu, X.; Chen, F.; Li, K.; Duan, Y. Effect of Various Oxidants on Reaction Mechanisms, Self-Limiting Natures and Structural Characteristics of Al_2O_3 Films Grown by Atomic Layer Deposition. *Adv. Mater. Interfaces* **2018**, *5*, 1701248. [CrossRef]
45. Kim, S.; Lee, S.H.; Jo, I.H.; Seo, J.; Yoo, Y.E.; Kim, J.H. Influence of Growth Temperature on Dielectric Strength of Al_2O_3 Thin Films Prepared via Atomic Layer Deposition at Low Temperature. *Sci. Rep.* **2022**, *12*, 5124. [CrossRef] [PubMed]